Steady Laminar Axisymmetrical Nozzle Flow at Moderate Reynolds Numbers: Modeling and Experiment

X. Grandchamp

Y. Fujiso

B. Wu

A. Van Hirtum[1]

e-mail: annemie.vanhirtum@gipsa-lab.grenoble-inp.fr

GIPSA-lab,
UMR CNRS 5216,
Grenoble University,
Grenoble, 38000 France

Flow through an axisymmetrical parameterized contraction nozzle of limited size with area contraction ratio 21.8 and total length 6 cm is studied for moderate Reynolds numbers $300 < Re < 20{,}200$. The transverse flow profiles at the nozzle exit are characterized by hot film anemometry for two different spatial step sizes. The flow at the exit is laminar and uniform in its core. Boundary layer characteristics at the nozzle exit are estimated from the transverse velocity profiles. Flow throughout the nozzle is modeled by implementing Thwaites laminar axisymmetrical boundary layer solutions in an iterative algorithm for which both universal functions, describing the shape factor and skin friction parameters respectively, are altered by adding a constant. The value of the constants is determined by fitting the modified universal functions to tabulated values reported in Blevins (Blevins, R., 1992, Applied Fluid Dynamics Handbook. Krieger, Malabar, FL.). The model is validated on the measured data. Adding nonzero constants to the universal functions improves the prediction of boundary layer characteristics so that the range of Reynolds numbers for which the discrepancy with experimental findings is less than 4% is extended from $Re > 3000$ to $Re > 1000$. Therefore, the studied contraction nozzle is of use for applications requiring a small nozzle with known low turbulence flow at the exit such as moderate Reynolds number free jet studies or bio fluid mechanics (respiration, speech production,…) and the flow at the exit of the nozzle can be accurately described by a simple boundary layer algorithm for $Re > 1000$. [DOI: 10.1115/1.4005690]

1 Introduction

Studies dealing with wind tunnel design are multiple and require to study the influence of the upstream geometry on the flow characteristics at the inlet of a wind tunnel working section [1–9]. Besides characterization of the exit profile of the nozzle, corresponding to the inlet portion to the working section, attention is given to avoid adverse pressure gradients along the nozzle walls in order to favor low turbulence inflow to the working section. Despite the amount of available literature most of the cited studies focus on wind tunnel applications in aeronautics so that even low-speed wind tunnels such as proposed in Ref. [4] are characterized by a typical exit diameter of 3 m and Reynolds number of 1.3×10^7. Consequently, the nozzle design and associated flow conditions at the nozzle exit reported in literature need to be validated for axisymmetrical inlet nozzles for which the exit diameter is of order of centimeters and for which the working range is limited to moderate Reynolds numbers of order 10^3. More recently, studies dealing with moderate Reynolds number free axisymmetrical jet development issuing from a contraction nozzle suggest that the velocity profile at the exit exhibits the sought features of uniform core and low turbulence level [10,11]. Nevertheless a thorough validation is necessary since the mentioned studies (1) provide a poor description of the contraction nozzle such as [10] where a contraction nozzle with exit diameter 4cm is mounted into a wall which is likely to alter results for Reynolds numbers $850 \leq Re \leq 6750$ and/or (2) are limited to a small range of Reynolds numbers such as in Ref. [11] where a single Reynolds number $Re = 16{,}000$ is experimentally assessed for a nozzle with exit diameter 14 mm and/or (3) uses commercially available nozzles such as in Ref. [12] for which the design is fixed and the smallest diameter is about 5 cm and for which flow features are not maintained for Reynolds numbers lower than $Re \approx 6500$.

Therefore, the current study aims to provide an axisymmetric contraction nozzle geometry based on the elegant parameterized geometries developed for wind tunnels [3,4] and to quantify flow features at the nozzle exit with respect to turbulence intensity and uniformity in the center. Those features are required as inlet conditions for experimental studies of free jets [10–12], aeroacoustics or bio fluid mechanics (respiration, speech production, whizzle,…). The mentioned examples of bio fluid mechanics are demanding since airflow is characterized by Reynolds numbers $Re < 20{,}200$, Mach number <0.2 and characteristic dimensions which are smaller than the smallest commercially available nozzle. Consequently, experimental validation of physical modeling of flow development and aeroacoustic noise production in relation to the vocal tract requires a tailored nozzle with known inlet conditions for low to moderate Reynolds numbers. Obviously, known inflow conditions can be simply obtained by inserting a pipe in the experimental setup in order to ensure fully developed Poiseuille flow. Nevertheless, for the aimed range of Reynolds numbers the required pipe length results in a long experimental setup (orders of meters [13–15] compared to order of centimeters for the length of an adult vocal tract [16–18]). In addition, pipe flow results in turbulence levels of 5% which is high compared to the level expected at the exit of a contraction nozzle [10,11,19,20]. Consequently, pipe flow is not suitable in case a short nozzle with low turbulence inflow is aimed. Instead, a short contraction nozzle is sought based on the parameterized geometries and design criteria proposed in Refs. [3,4].

In order to quantify flow properties at the nozzle exit experimentally, the transverse velocity profile at the exit of the axisymmetrical contraction nozzle is measured by hot-film anemometry from which the flow at the nozzle exit is characterized and boundary layer characteristics are derived [19–22]. In addition, the influence

[1]Corresponding author.

Contributed by Fluids Engineering Division for the JOURNAL OF FLUIDS ENGINEERING. Manuscript received February 2, 2011; final manuscript received November 15, 2011; published online February 23, 2012. Assoc. Editor: Mark F. Tachie.

of the transverse spatial step on the estimated boundary layer characteristics is assessed.

Besides an experimental validation it is sought to model the flow properties at the nozzle exit and to validate the outcome on the measured quantities. In addition, flow modeling can be used to assess the variation of geometrical nozzle parameters on the flow properties at the nozzle exit and to describe the flow throughout the nozzle. Since a flow with uniform center and low turbulence intensity is aimed, it is appropriate to apply laminar boundary layer theory. A simple and accurate model [19,20,22] is provided by Thwaites laminar axisymmetrical boundary layer solution [23–25]. The accuracy of the model is further increased by implementation in an iterative algorithm. Thwaites method exploits a functional relationship between Thwaites parameter and the boundary layer shape factor and skin friction parameter which varies as function of flow and geometrical conditions and is expressed either by tabulated values, e.g., [1] or by universal functions, e.g., [22]. Consequently, validation of the model results should take into account different functional relationships. In order to do so, it is proposed to alter the universal functions describing the shape factor and skin friction parameter by adding a constant to each function. The value of the constants is determined by fitting the modified universal functions to the tabulated values [1].

In the following, the nozzle geometry is motivated. Next, Thwaites laminar boundary layer solution is outlined, the modified universal functions are introduced and the iterative algorithm is detailed. In the following section, the experimental setup is described and the measured flow profiles at the nozzle exit are characterized. Next, the flow throughout the nozzle is modeled and experimental and modeled flow results are compared. Finally, main findings are summarized in the conclusion.

2 Nozzle Geometry

An axisymmetrical contraction nozzle is needed to provide air inflow with reduced turbulence level and uniformity [3,4,9]. Moreover a small nozzle is preferred in order to facilitate the use in an experimental setup. The axisymmetrical contraction nozzle geometry proposed in Ref. [3] is applied. The nozzle radius $R(x)$ along the contraction is fully defined by two matched cubics as:

$$R(x) = \left(\frac{D_1}{2} - \frac{D_2}{2}\right)\left(1 - \frac{(x/L)^3}{(x_m/L)^2}\right) + \frac{D_2}{2}, \quad x \le x_m \tag{1}$$

$$R(x) = \left(\frac{D_1}{2} - \frac{D_2}{2}\right)\frac{(1 - x/L)^3}{(1 - x_m/L)^2} + \frac{D_2}{2}, \quad x > x_m \tag{2}$$

with x the main streamwise direction, matching point of the cubics x_m, inlet diameter D_1, outlet diameter D_2 and total nozzle length L. Consequently, the nozzle geometry is fully determined by four geometrical parameters (D_1, D_2, L, x_m) compared to six parameters required for the contour nozzle proposed in Ref. [4]. The geometrical parameter set (D_1, D_2, L, x_m) is equivalent to ($D_{1,2}$, CR, L, x_m) with CR denoting the area contraction ratio defined as $CR = (D_2/D_1)^2$.

The exit diameter D_2 is determined based on the aimed flow conditions of moderate Reynolds numbers $300 < Re < 20{,}200$ and low Mach number <0.2. Consequently, characteristic lengths are smaller than 20mm so that the outlet diameter D_2 yields 20 to 25 mm, $20 \le D_2 \le 25$ mm. From studies of the contraction ratio in relation to the Reynolds number [3,4], it is known that large contraction ratios are more tolerant to irregularities occurring for low velocities due to, e.g., flow separation. Therefore the inlet diameter D_1 is set to $D_1 = 100$ mm resulting in a large area contraction ratio $15 \le CR \le 22$. The total nozzle length is set to 0.6 times the inlet diameter D_1 or $L = 60$ mm[3]. Due to the high contraction ratio CR a short outlet length is needed to avoid boundary layer thickening at the exit. Therefore, the matching point is chosen as $x_m = 52$ mm, corresponding to $x_m = 0.86L$, so that the outlet length is less than 5 mm. The resulting nozzle geometry is illustrated in Fig. 1 for geometrical parameters $D_1 = 100$ mm, $D_2 = 25$ mm, $L = 60$ mm, and $x_m = 52$ mm.

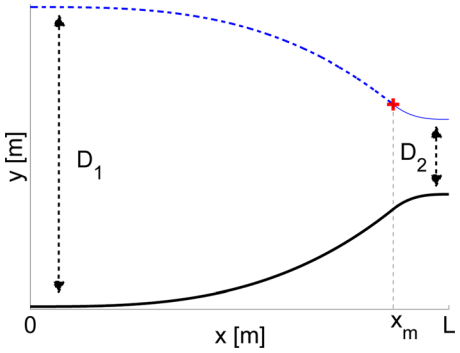

Fig. 1 Illustration of parameterized axisymmetrical nozzle geometry, $D(x) = 2R(x)$, obtained from matching at $x = x_m$ an upstream cubic (1) (dashed line) and a downstream cubic (2) (thin full line) with parameters $D_1 = 100$ mm, $D_2 = 25$ mm, $L = 60$ mm, and $x_m = 52$mm. The longitudinal x-axis corresponds to the main streamwise direction and the y-axis to the transverse direction.

3 Laminar Boundary Layer Flow Modeling

At moderate Reynolds numbers the region in which viscous forces are important is confined to a thin laminar boundary layer adjacent to the wall. The resulting boundary layer theory in presence of a pressure gradient is described by the Von Kármán momentum integral equation for steady flows [19,20]. The development of the laminar boundary layer on the walls of the contraction defined in the previous section is estimated by Thwaites method to solve the momentum integral equation for laminar, incompressible and axisymmetrical boundary layers [23–25]. Outside the boundary layer, the flow is described as an inviscid irrotational ideal fluid flow in a channel. In the following $U(x)$ denotes the fluid flow velocity outside the boundary layer and $u(x, y)$ indicates the velocity in the boundary layer.

The flow in the contraction is modeled by calculation of the laminar boundary-layer momentum thickness,

$$\delta_2(x) = \int_0^\infty \frac{u(x, y)}{U(x)}\left(1 - \frac{u(x, y)}{U(x)}\right) dy \tag{3}$$

as a function of downstream distance x with Thwaites equation using quasi-similarity assumptions [19,24]:

$$\delta_2^2(x)R^2(x)U^6(x) - \delta_2^2(0)R^2(0)U^6(0) = 0.45\nu\int_0^x R^2(x)U^5(x)dx \tag{4}$$

where $U(0)$, $\delta_2(0)$ and $R(0)$ are the flow velocity, momentum thickness and radius at the nozzle inlet $x = 0$ and ν the kinematic viscosity. The second term at the left hand side of Eq. (4) takes into account initial conditions at $x = 0$.

Next, a dimensionless Thwaites parameter λ is defined as

$$\lambda = -\frac{\delta_2^2}{\nu}\frac{\partial U(x)}{\partial x} \tag{5}$$

from which a skin friction parameter $S(\lambda)$,

$$S(\lambda) = \frac{\delta_2}{U(x)}\frac{\partial U}{\partial y} \tag{6}$$

and boundary layer shape parameter $H(\lambda)$,

$$H(\lambda) = \frac{\delta_1(x)}{\delta_2(x)} \tag{7}$$

can be estimated and for which δ_1 denotes the displacement thickness,

$$\delta_1(x) = \int_0^\infty \left(1 - \frac{u(x, y)}{U(x)}\right) dy \tag{8}$$

Note that since the wall shear stress is defined as $\tau = \rho\nu\frac{\partial U}{\partial y}$, with ρ denoting the fluid density, also the following holds:

$$S(\lambda) = \frac{\tau\delta_2}{\rho\nu U} \tag{9}$$

Consequently, the wall shear stress can be derived from the skin friction parameter $S(\lambda)$ which becomes zero at flow separation and depends only on the dimensionless Thwaites parameter λ.

The skin friction parameter $S(\lambda)$ and shape parameter $H(\lambda)$ reported in literature are derived from experimental data and presented as tabulated values [1] or as universal Thwaites functions [22,26]. It is observed that a discrepancy exists between the tabulated and functional values [1,22,26]. Non zero constants $c_H = 0.35$ and $c_S = -0.02$ need to be added to the universal Thwaites functions [22,26] in order to accurately fit the tabulated values reported in Ref. [1]. The accuracy of the fit is confirmed by the coefficient of determination which yields 0.97. The resulting modified universal Thwaites functions are

$$S(\lambda) = 1.8\lambda^2 + 1.57\lambda + 0.22 + c_S, \quad 0 \le \lambda \le 0.1 \tag{10}$$

$$H(\lambda) = 5.24\lambda^2 - 3.75\lambda + 2.61 + c_H \tag{11}$$

$$S(\lambda) = \frac{0.018\lambda}{0.107 + \lambda} + 1.402\lambda + 0.22 + c_S, \quad -0.1 \le \lambda \le 0 \tag{12}$$

$$H(\lambda) = \frac{0.0731}{0.14 + \lambda} + 2.088 + c_H \tag{13}$$

where the constants $c_{H,S}$ are introduced to account for different flow and geometrical conditions. Moreover from the cited studies it is seen that the constants can vary in the range $0 \le c_H \le 0.35$ and $-0.02 \le c_S \le 0$. Resulting values for $H(\lambda)$ and $S(\lambda)$ obtained from the modified universal Thwaites functions for zero and non-zero constants $c_{H,S}$ are illustrated in Fig. 2.

Using nonzero constants ($c_H = 0.35$ and $c_S = -0.02$) instead of zero constants ($c_{H,S} = 0$) is therefore seen to alter H and S significantly since H increases between 10 and 25% and S decreases between 5% and 10%. Therefore, the constants directly influence the underlying physics since accounting for the set of non zero constants in the modeling facilitates flow separation.

Therefore, the influence of two sets of constants $c_{H,S}$, zero ($c_{H,S} = 0$) and non zero ($c_H = 0.35$ and $c_S = -0.02$), on the modeling outcome is assessed for flow through the nozzle outlined in Sec. 2. In addition, the model outcome will be compared to experimental data.

The equations outlined in this section are implemented in an iterative algorithm detailed in the flow chart given in appendix 6 which is applied at each spatial position until the solution converges for λ and U. Briefly, the velocity is initialised using the given volume flow rate Q and geometrical radius $R(x)$ from which a first estimation of the momentum thickness δ_2 is obtained so that the Thwaites parameter λ and the displacement thickness δ_1 can be estimated by using the expression for $H(\lambda)$ given in Eq. (7). The velocity is than re-estimated while accounting for the displacement thickness from which the values of λ and U are updated by relaxation and the shear stress τ is estimated with the expression of $S(\lambda)$ in Eq. (6). In order to increase the accuracy of the model approach, the procedure is repeated until the retrieved values for U and λ converges to within 0.01%.

4 Experimental Setup and Flow Characterization

In order to validate the model outcome and to characterize the velocity profile at the nozzle outlet, hot film anemometry measurements are performed at the exit. In the following the experimental setup and procedure are described and the measured velocity profiles are characterized.

4.1 Experimental Setup. The experimental setup is illustrated in Fig. 3(*a*). It consists in an oil injected rotary screw compressor Copco GA7 with an integrated oil/water separator. In addition, liquid and solid particles as well as oil odors and vapors are filtered (Copco & Beko DD17, PD17, QD17) out so that dry air with no oil particulates is delivered. In addition, the compressor is equipped with an air receiver of 300 l.

To avoid any resulting vibrations and flow disturbances, the compressor [a] is isolated in a separated room. Downstream, a pressure regulator [b] (Norgren type 11-818-987) and a manual valve [c] are placed in order to reduce air pressure and prevent pressure fluctuations during experiments. The pressure regulator is connected with a thermal mass flow meter (TSI 4040) [d] via a

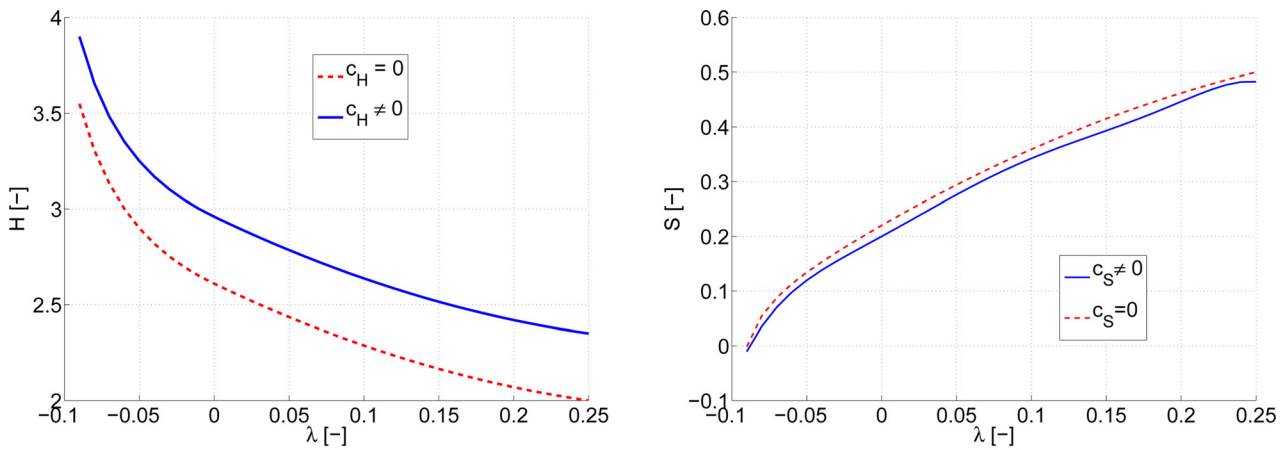

(a) $H(\lambda, c_H)$ (b) $S(\lambda, c_S)$

Fig. 2 Illustration of (*a*) $H(\lambda)$ for $c_H = 0$ ($c = 0$) and $c_H = 0.35$ ($c \neq 0$) and (*b*) $S(\lambda)$ for $c_S = 0$ ($c = 0$) and $c_S = -0.02$ ($c \neq 0$)

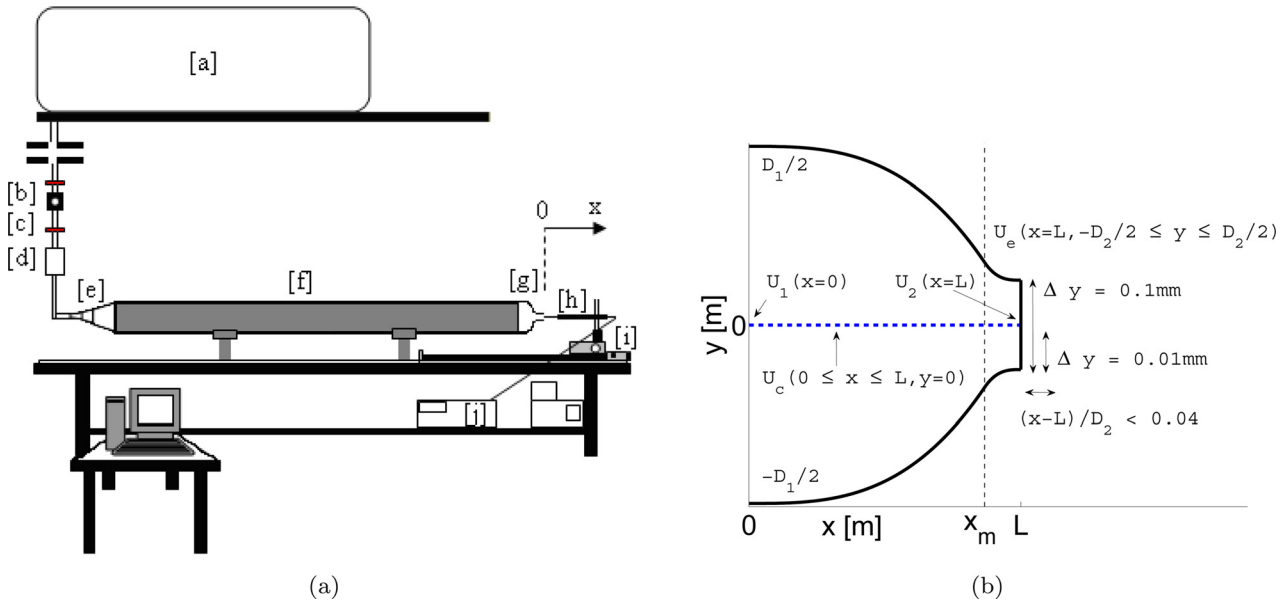

Fig. 3 (*a*) A sketch of the apparatus: [a] air supply, [b] pressure regulator, [c] valve, [d] mass flow meter, [e] divergent, [f] uniform pipe, [g] convergent nozzle with parameters D_1=100mm, D_2=21.4mm, L=60mm and x_m=52mm, [h] hot film, [i] positioning system, [j] IFA 300. (*b*) Detail of the experimental nozzle and velocities of interest: centerline velocity $U_c(x, y=0)$, centerline velocity at the inlet $U_1 = U_c(x=0, y=0)$ and centerline velocity at exit $U_2 = U_c(x=L, y=0)$. The transverse velocity at the nozzle exit $U_e(y)$ is measured at a small distance from the nozzle exit $(x-L)/D_2 < 0.04$. The complete wall to wall exit velocity profile is measured with a transverse spatial step size of $\Delta y = 0.1$ mm further labeled 'measured exit profile'. A second partial profile is measured near the wall covering the boundary layer with a precise transverse spatial step size $\Delta y = 0.01$ mm further labeled "measured exit boundary layer" profile.

uniform duct of diameter 0.01 m. Then, the air circulates through a concatenation of diffusers [e]. In order to limit flow separation, diffusers are filled with steel wool and a first grid with 1mm diameter holes is positioned at 2/3 of the total length of the divergent inlet section. A uniform pipe diameter with diameter 0.1 m and length 2 m [f], separating the concatenation of diffusers from the convergent nozzle [g], is used as a settling chamber to ensure total flow mixing and contains a second perforated plate at its entrance.

The experimental nozzle is detailed in Fig. 3(*b*). The nozzle's geometry is designed as outlined in Sec. 2 and fully described by the geometrical parameter set of inlet diameter $D_1 = 100$ mm, outlet diameter $D_2 = 21.4$ mm, total length $L = 60$ mm and matching point $x_m = 52$ mm. The experimental nozzle exit presents an area of 0.00036 m^2, imposing on the air an area contraction ratio $CR = 21.8$.

The transverse velocity at the nozzle outlet is measured by hot film anemometry. The hot film [h] (TSI 1201-20; diameter of $d_w = 50.8$ μm and a working length of 1.02 mm) is placed at a distance $(x-L)/D_2 < 0.04$ downstream of the nozzle exit as shown in Fig. 3(*b*). The applied streamwise position is in accordance with Refs. [10,11]. In order to measure the transverse exit velocity profile, the probe is mounted on a two-dimensional stage positioning system [i] (Chuo Precisio Industrial Co. CAT-C, ALS-250-C2P and ALS-115-E1P), providing a positioning accuracy in the radial y-direction perpendicular to the airflow of 2 μm. The probe displacement is controlled by a user-defined matrix implemented in LabVIEW (National Instruments). At each measurement station, the hot-film output voltage E_{meas} is collected by a constant temperature anemometer system [j] (TSI IFA 300) and stored on a computer. The room temperature at the beginning of each velocity profile measurement is controlled thanks to an air conditioning system in order to minimize temperature variations. To account for drift in room temperature T_a from the reference ambient temperature, $T_{a,r} = 21.5\,^{\circ}$C, the measured hot-film output voltages E_{meas} are corrected to E_{corr} [27], with T_f denoting the airflow temperature:

$$E_{corr} = E_{meas}\left(\frac{T_f - T_a}{T_f - T_{a,r}}\right)^{-1/2} \tag{14}$$

The velocity is derived from the measured voltages E_{corr} following the calibration procedure outlined in Ref. [28] resulting in a calibration curve fitted on a fourth order polynomial law. The calibration procedure consists in an iterative approach based on the displacement thickness so that boundary layer development is accounted for. The calibration error is due to the experimental error on the measured volume flow rates. As such the calibration method is shown to improve the calibration for low velocities up to 30% compared to other iterative methods such as described in Ref. [15]. Consequently the applied calibration procedure is particularly suitable for moderate Reynolds numbers dealt with in the current study. It is shown in Ref. [28] that the calibration error is due to the experimental error on the measured volume flow rates, so that the error on the measured instantaneous velocities is smaller than 1% for velocities >1.4 m/s and smaller than 5% for velocities between 0.17 and 1.4 m/s.

Besides the experimental error, a statistical error analysis is performed in order to estimate the error on the mean velocity and local turbulence intensity determined from the measured instantaneous velocities at each measurement position and accounting for the data sampling at 40 kHz during 4s [29]. The statistical error follows from a Reynolds decomposition and further assuming that the fluctuating portion is described by a Gaussian law distributed around zero for which the variance is directly related to the turbulence intensity defined as $T_U = \sigma/U_e$, with σ denoting the root mean square velocity:

$$\sigma = \sqrt{\frac{1}{N_{tot}}\sum_{p=1}^{N_{tot}}(U_e^p - U_e)^2} \tag{15}$$

where N_{tot} denotes the total number of instantaneous measured velocities U_e^p and U_e denotes the mean velocity. The statistical error on the estimated mean velocity U_e yields $\sigma/\sqrt{N_{ind}}$ and on the estimated turbulence intensity T_U yields $U_e^2/2N_{ind}$ with N_{ind} the number of independent samples [30]. The number of independent samples is approximated as the ratio between the acquisition time

Table 1 Relevant measurement range and corresponding uncertainties of instruments. Upper limits of uncertainties for measured instantaneous velocities and estimated statistical errors for the first and second velocity moments [28–30] for sampling at 40kHz during 4s. Statistical errors are estimated assuming 2% turbulence level, i.e., $T_U = 2\%$.

Instruments				
Quantity	Symbol	Instrument	Relevant measurement range	Uncertainty
Flow rate	Q	TSI model 4040	5–305 l/min	±2%
Fluid temperature	T_f	TSI model 4040	20–25 °C	±1 °C
Room temperature	T_a	OTAX 421001	22–25 °C	±0.2 °C
Nozzle exit diameter	D_2	Manufacturing precision	21.4 mm	±0.02 mm
Fluid pressure	P_f	TSI model 4040	97–115 kPa	±1 kPa
Data acquisition	E_{meas}	PCI-MIO-16XE-10 (National Instruments) and IFA300 (TSI)	±10V	±72.3μV
Transverse positioning	Δy	CHUO Precisio	0.1 mm and 0.01 mm	±0.002 mm

Velocities				
Velocity	Symbol	Error	Relevant range	Uncertainty
Instantaneous velocity	U^p	measurement error on Q	> 1.4m/s	$< 1\%$
Mean velocity	U_e		> 0.17m/s and < 1.4m/s	$< 5\%$
Root mean square velocity	σ		< 0.17m/s	$> 5\%$

of 4s and the integral time $\approx D_2/U_e$, i.e., $N_{ind} \approx 8Q/\pi D_2^3$. The resulting statistical errors for an assumed turbulence level of 2% is smaller than the experimental measurement error. It is shown in the following section, Fig. 5, describing the measured velocity profiles, that 2% overestimates the measured turbulence level along the centerline at the exit. Therefore, the measurement error on the volume flow velocity is the main error source in the performed measurements.

All used instruments, their corresponding uncertainties and the error estimations on the measured velocity and statistical quantities are summarized in Table 1.

4.2 Measured Velocity Profiles at the Nozzle Exit. Transverse flow characteristics at the nozzle exit are measured by placing the probe at the horizontal centerline of the jet at a distance $(x-L)/D_2 < 0.04$ and displacing the probe in the transverse direction as schematically illustrated in Fig. 3(*b*). The streamwise positioning $(x-L)/D_2 < 0.04$ in order to measure the transverse flow at the nozzle exit is commonly used in literature, *e.g.* $(x-L)/D_2 < 0.04$ in [10] or $(x-L)/D_2 = 0.05$ in Ref. [11]. Volume flow rates are varied in the range $5 < Q < 305$l/min, which corresponds to Reynolds numbers $300 < Re < 20{,}200$ with Re the Reynolds number based on the bulk velocity at the nozzle exit, i.e., $Re = 4Q/\nu\pi D_2$.

For each Reynolds number two transverse profiles are measured with different spatial step sizes. The spatial step sizes are chosen relative to the hot film diameter, $d_w = 50.8\ \mu$m ≈ 0.05 mm, since it is expected that the accuracy of the step size relative to the sensor diameter will affect the accuracy of the numerical integration required in order to determine the boundary layer characteristics at the nozzle exit such as δ_1 and δ_2 defined in Eq. (8) and Eq. (3). Firstly, the transverse exit profile is measured from wall to wall, $-0.5 \le y/D_2 < 0.5$, with a transverse spatial step equal to $\Delta y = 0.1$mm, i.e., $\Delta y > d_w$ since $\Delta y \approx 2d_w$, further labeled "measured exit" profile. Secondly, a boundary layer profile is measured with a spatial step $\Delta y = 0.01$ mm, i.e., $\Delta y < d_w$ since $\Delta y \approx d_w/5$, further labeled "measured exit boundary layer" profile. Finally, it is remarked that the spatial step size used to measure the transverse exit profile is not mentioned in the cited studies [10,11].

Measured velocity profiles obtained with spatial steps $\Delta y = 0.1$ mm and $\Delta y = 0.01$ mm are illustrated in Fig. 4(*b*) for $-0.5 \le R/D_2 \le -0.3$.

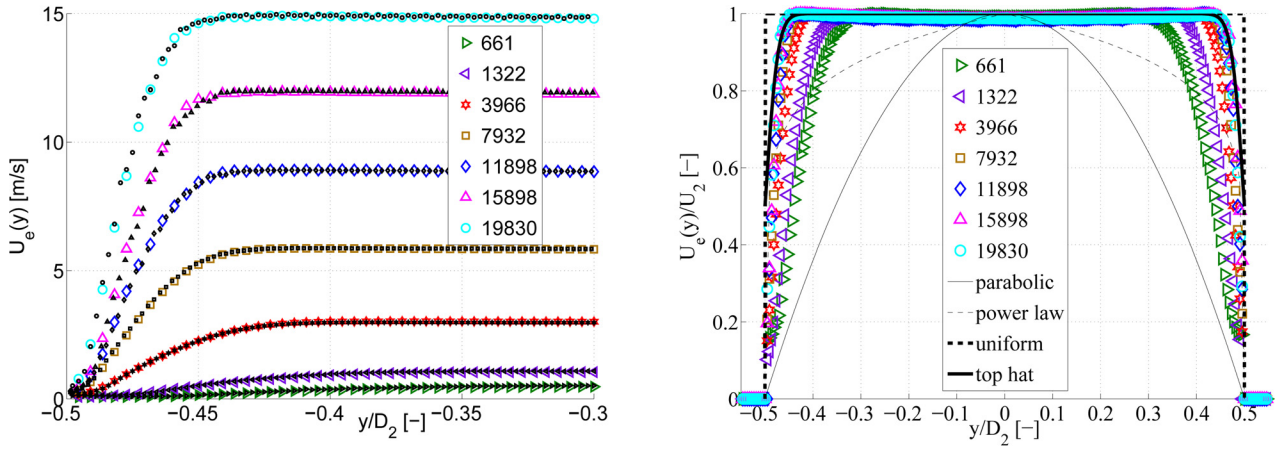

(a) $\Delta y = 0.1$mm and $\Delta y = 0.01$mm (b) $\Delta y = 0.1$mm

Fig. 4 (*a*) Comparison of measured exit velocity profiles $U_e(y)$ obtained with spatial step $\Delta y = 0.1$ mm (symbols) and measured exit boundary layer profiles $\Delta y = 0.01$ mm (dots) for different Reynolds numbers Re in the range $-0.5 \le R/D_2 \le -0.3$. (*b*) Measured normalized transverse exit velocity profiles $U_e(y)/U_2$ for $\Delta y = 0.1$mm and comparison with parabolic, 1/7 power law, uniform profile with vanishing momentum thickness $\delta_2 = 0$ and top hat profile with momentum thickness $\delta_2 = 0.004D_2$.

The measured velocity profiles match well for all assessed Reynolds numbers illustrating that no error is due to the positioning of the hot film at $(x-L)/D_2 < 0.04$.

Normalized mean exit velocity profiles $U_e(y)/U_2$ with U_2 the exit centerline velocity, are illustrated in Fig. 4(*b*). The measured exit profiles are compared to a parabolic velocity profile describing fully developed pipe flow in Eq. (16), a 1/7 power law profile describing turbulent flow in Eq. (17), a theoretical uniform profile corresponding to a top hat velocity profile in Eq. (18) with vanishing momentum thickness $\delta_2 = 0$ [31] and a top hat profile accounting for boundary layer development with momentum thickness $\delta_2 = 0.004 D_2$:

$$U_e = U_2\left(1 - \left(\frac{2|y|}{D_2}\right)^2\right) \tag{16}$$

$$U_e = U_2\left(1 - \frac{2|y|}{D_2}\right)^{1/7} \tag{17}$$

$$U_e = \frac{1}{2}U_2\left(1 - \tanh\left(\frac{D_2}{8\delta_2}\left(\frac{2|y|}{D_2} - \frac{D_2}{2|y|}\right)^2\right)\right) \tag{18}$$

For all assessed Reynolds numbers the variation in mean velocity is lower than 0.5% in the center portion of the jet $|y|/D_2 < 0.25$. The top hat profile describes well the uniform flow in the constant velocity center region as well as the boundary layer region in case a non vanishing momentum thickness is accounted for $\delta_2 \neq 0$. Nevertheless, it is seen that the boundary layer thickness increases rapidly for $Re < 3000$. For Reynolds numbers $Re > 3000$ the constant velocity region is extended to $|y|/D_2 < 0.4$ in accordance with observations described by Ref. [10,11]. A small overshoot in the outer part of the core of the mean exit velocity profiles is observed. The overshoot is of the order of magnitude reported in Ref. [11] and smaller than the overshoot observed in Ref. [10]. The contraction nozzle studied by Ref. [10] has no outlet length, i.e., nozzle outlet for which the nozzle is parallel with the centerline, which causes the vena contracta effect to be more pronounced in the exit profile. The overshoot might also be effected due to differences in contraction ratio. The contraction ratios in the current study and in Ref. [11] are of the same order of magnitude whereas information on the contraction ratio of the nozzle used in Ref. [10] is missing.

Turbulence intensities $T_U = \frac{\sigma}{U_2}$ derived on the measured exit velocity profiles are presented in Fig. 5.

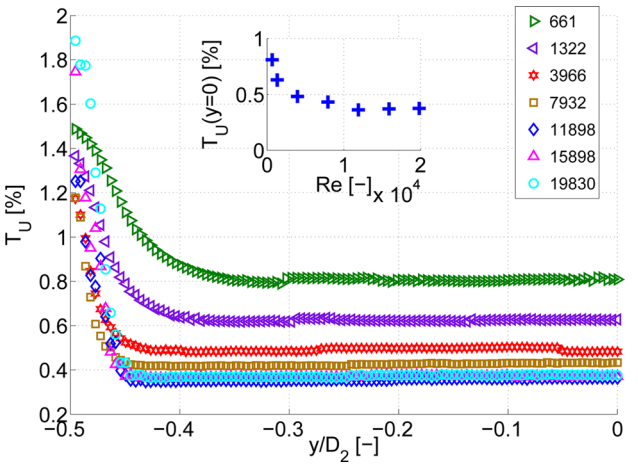

Fig. 5 Measured turbulence intensities $T_U \times 100$ [%] of exit velocity profiles for $\Delta y = 0.1$ mm. In the inner plot, measured centerline turbulence intensities $T_U(y=0)$ are presented as function Reynolds number *Re*.

The centerline turbulence intensities T_U $(y=0)$ vary between 0.4% and 1% for all assessed Reynolds numbers and are smaller than 0.6% for Reynolds number $Re > 3000$. This very low centerline turbulence level agrees well with the measurements reported in Refs. [10,11]. The centerline turbulence intensities decreases with Reynolds number as was also observed by Ref. [10]. Away from the centerline the turbulence intensities are seen to be constant throughout the constant region of the mean velocity exit profile. In the boundary layer the turbulence intensity T_U increases and vary in the range of 1.2% up to 1.9%. Retrieved T_U values are again of the same order of magnitude as reported in Refs. [10,11]. In the cited studies [10,11] the turbulence intensity as function of the exit diameter is shown for one single Reynolds number so that no comparison can be made for the found variation with Reynolds number. Nevertheless, the variation is likely due to the error which becomes large when the velocity approaches zero. Despite this variation the maximum centerline turbulence level is low, i.e., lower than 1%, so that the boundary layer is laminar. In order to further determine the nature of the boundary layer the measured boundary layer profiles are compared to the laminar Blasius profile. The measured boundary layer profiles approximate well Blasius laminar boundary layer profile as illustrated in Fig. 6(*a*)

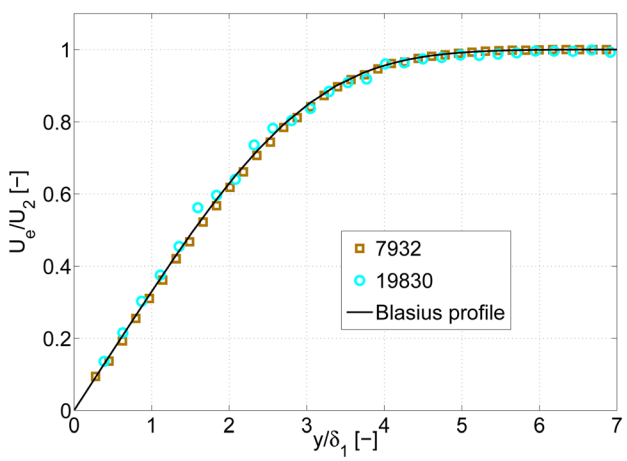

(a)

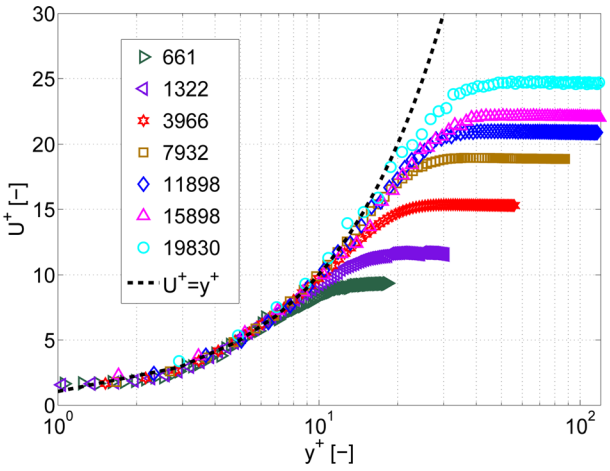

(b)

Fig. 6 Boundary layer characterization of the measured mean boundary layer profiles for $\Delta y = 0.01$ mm: (*a*) comparison with Blasius profile for a laminar boundary layer. (*b*) Comparison of $U^+(y^+)$ with linear law of the wall $U^+ = y^+$ for a laminar boundary layer.

confirming the laminar nature of the boundary layer [19,20]. In addition, in Fig. 6(*b*) the measured boundary layer profiles are seen to be in very good agreement with a linear law of the wall defined as $U^+ = y^+$ with U^+ denoting the velocity normalized by the friction velocity $U_\tau = \sqrt{\tau/\rho}$ and y^+ indicating the Reynolds number based on the friction velocity U_τ and distance from the wall, i.e., $y + D/2$ [20,22,32].

So from the measured velocity profiles, it is observed that the flow at the nozzle exit is laminar and the boundary layer is seen to be confined to the vicinity of the wall for all assessed Reynolds numbers *Re* so that the mean velocity profile has a satisfactory sharp top-hat shape.

5 Nozzle Flow: Modeling and Experiment

In the current section flow through an axisymmetrical nozzle is discussed for Reynolds numbers in the range $300 < Re < 20{,}200$. The flow through the nozzle is modeled following the laminar boundary layer method outlined in Sec. 3. The model outcome is discussed in Sec. 5.1. Next, the influence of geometrical and model parameters on the modeled centerline velocity at the nozzle exit is assessed in Sec. 5.2. In addition, modeled and measured centerline velocities at the exit of the nozzle are compared. Finally, the experimental validation of boundary layer characteristics at the nozzle exit is presented in Sec. 5.3.

5.1 Modeled Streamwise Nozzle Flow. The flow through an axisymmetrical nozzle is modeled following the laminar boundary layer method outlined in Sec. 3. The constants $c_{H,S}$ introduced in the modified universal Thwaites functions defined in Eq. (13) are set to zero so that $c_H = 0$ and $c_S = 0$. The nozzle geometry $A(x) = \pi R(x)^2$ is obtained as outlined in Sec. 2 and consequently fully defined by the parameter set (D_1, D_2, L, x_m) composed out of inlet diameter D_1, outlet diameter D_2, total nozzle length L and streamwise position of matching point x_m. In the current section the parameter set is fixed to the values corresponding to the experimental nozzle: $D_1 = 100$ mm, $D_2 = 21.4$ mm, $L = 60$ mm, and $x_m = 52$ mm. The influence of non zero constants on the model outcome and of varying geometrical nozzle parameters on the modeled flow outcome at the nozzle exit is discussed in Sec. 5.2. The modeled streamwise flow quantities for Reynolds numbers in the range $300 < Re < 20{,}200$ are illustrated in Fig. 7.

The modeled mean streamwise centerline velocities normalized by the inlet velocity, U_c/U_1, are illustrated in Fig. 7(*a*). The centerline velocity increases in the streamwise direction until a maximum is reached at the nozzle exit. As a benchmark the modeled centerline velocity is compared to the bulk velocity, defined as the ratio of volume flow rate Q and area $A(x)$, corresponding to an ideal fluid for which boundary layer development is neglected which results in $U(x)/U_1 = A_{x=0}/A(x)$. Consequently, the normalized bulk velocity depends only on the geometry and not on the Reynolds number *Re*. At the nozzle outlet the bulk velocity equals the area contraction ratio *CR*. From Fig. 7(*a*) is seen that the normalized modeled centerline velocity profiles collapse to a single curve for $Re > 3000$. For Reynolds numbers $Re < 3000$ on the other hand the ratio U_c/U_1 increases throughout the nozzle due to an increased flow acceleration for $Re < 3000$ as shown in Fig. 7(*b*) where the streamwise normalized flow acceleration $dU_c/dx \times D_1/U_1$ is plotted. The flow is accelerated due to the contraction geometry. Downstream the nozzle inlet, the flow accelerates gradually until a maximum acceleration is reached just downstream the matching point x_m. The position of maximum flow acceleration is defined by the geometry and independent from the Reynolds number *Re*. Downstream the maximum flow acceleration the flow acceleration reduces until the nozzle exit. As expected from the centerline velocity, the acceleration of all assessed Reynolds numbers collapses except for $Re < 3000$. The reduced flow acceleration is causing increased boundary layer development for low Reynolds numbers as was observed experimentally on the mean exit velocity profiles shown in Fig. 4(*a*) since a decrease of velocity leads to an increase of the viscous effects and consequently boundary layer thickening. Consequently, values characterizing the boundary layer such as the displacement thickness δ_1 and the momentum thickness δ_2 are expected to decrease as the Reynolds number increases.

The displacement thickness δ_1 normalized by the exit diameter D_2 is shown in Fig. 7(*c*). It is observed that the boundary layer develops in the almost uniform inlet section of the nozzle resulting in an increase of the displacement thickness δ_1. The displacement parameter δ_1 increases to 10% of the exit diameter D_2, corresponding to 2% of the inlet diameter D_1 for $Re > 3000$. For Reynolds numbers $Re < 3000$ the increase of δ_1 is more pronounced yielding 25% the exit diameter D_2 or 5% of the inlet diameter D_1. At the onset of the contraction δ_1 decreases due to the flow acceleration in the streamwise direction towards the matching point x_m imposing an increased flow velocity which reduces viscous effects and so the growth of the boundary layer. A minimum is reached at the point of maximum flow acceleration which is easily identified from Fig. 7(*b*). For all Reynolds numbers the displacement thickness is less than 3% at the streamwise location corresponding to maximum flow acceleration and less than 0.5% for $Re > 3000$. Downstream the point of maximum flow acceleration, the flow acceleration reduces towards the nozzle exit due to the reduced rate of area change. This results in a velocity reduction which is associated with an increase of viscous effects and so a boundary layer thickening. As a consequence, boundary layer parameters $\delta_{1,2}$ increase towards the nozzle exit. At the nozzle exit the discplacement thickness δ_1 yields less than 1% of the exit diameter D_2 for $Re > 3000$. For smaller Reynolds numbers $Re < 3000$, the displacement thickness δ_1 increases to 4% of the exit diameter D_2.

The normalized momentum thickness δ_2/D_2 is shown in Fig. 7(*d*). Comparing δ_1/D_2 shown in Fig. 7(*c*) to δ_2/D_2 represented in Fig. 7(*d*) shows that the tendencies outlined for the normalized displacement thickness δ_1/D_2 also apply to the normalized momentum thickness δ_2/D_2, except that the magnitude of δ_2 is reduced compared to the magnitude of δ_1. The ratio of δ_1 and δ_2, which corresponds to the shape factor H following Eq. (7), is shown in Fig. 7(*e*). For all assessed Reynolds numbers *Re*, the shape factor at the nozzle inlet yields $H = 2.96$, which is associated with a laminar flow. The shape factor H is seen to decrease throughout the nozzle with less than 0.5% so that $2.96 \geq H \geq 2.95$ holds throughout the nozzle. Consequently, streamwise variation of the boundary layer shape factor $H \approx 2.95$ is limited which is in accordance with the flow uniformity aimed for by using a contraction nozzle. The observed decrease in the shape factor with increasing Reynolds number *Re* is less than 0.05% which is of no significance when accounting for a model error and is of no significance with respect to the total range of the shape factor shown in Fig. 2. Therefore, the influence of Reynolds number on the boundary layer shape factor can be neglected.

From Eq. (7) is seen that the shape factor $H(\lambda)$ is only function of the Thwaites parameter λ. Consequently, an almost constant value of $H(\lambda)$ throughout the nozzle suggests an almost constant value for the skin friction parameter $S(\lambda)$, defined in Eq. (6), and suggests an almost constant value for the Thwaites parameter λ defined in Eq. (5). From Fig. 7(*g*) is seen that the skin friction parameter at the nozzle inlet yields $S = 0.2$ and increases throughout the nozzle with less than 3% so that $0.2 \leq S \leq 0.205$ holds throughout the nozzle. Consequently, streamwise variation of the skin friction parameter $S \approx 0.2$ is indeed limited. The small variation of S as function of Reynolds number at the nozzle exit is smaller than 0.5% which is of no significance when accounting for a model error and is of no significance with respect to the total range of the skin friction parameter shown in Fig. 2. Since $S > 0$ for all streamwise positions it is observed that the flow remains attached to the nozzle walls for all streamwise positions so that no flow separation occurs. Therefore, the proposed nozzle enables flow uniformity at the nozzle exit and no flow separation occurs upstream the nozzle exit. In accordance with the observations for

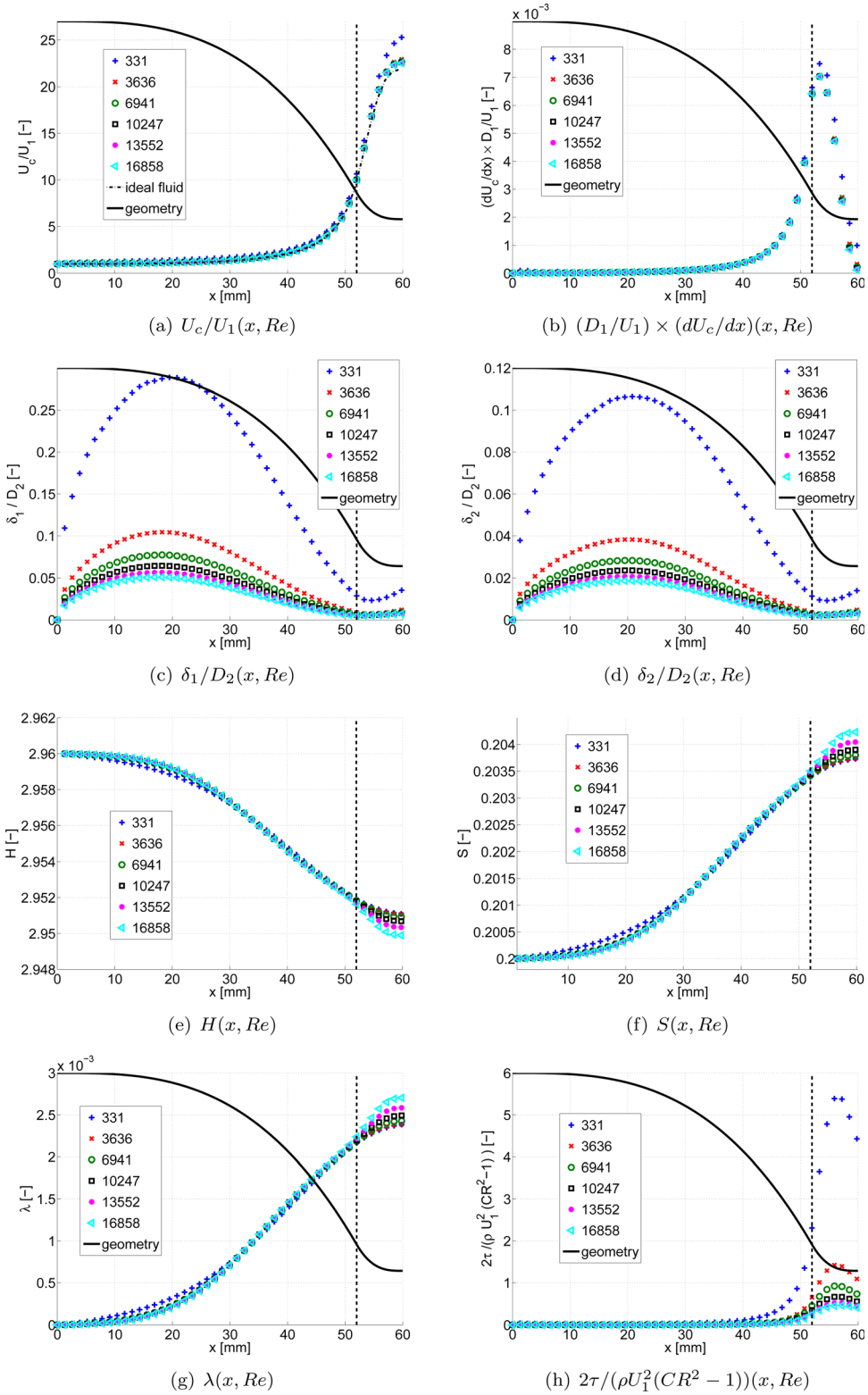

(a) $U_c/U_1(x, Re)$ (b) $(D_1/U_1) \times (dU_c/dx)(x, Re)$

(c) $\delta_1/D_2(x, Re)$ (d) $\delta_2/D_2(x, Re)$

(e) $H(x, Re)$ (f) $S(x, Re)$

(g) $\lambda(x, Re)$ (h) $2\tau/(\rho U_1^2(CR^2 - 1))(x, Re)$

Fig. 7 Illustration of modeled streamwise flow development through the contraction nozzle with parameters D_1=100 mm, D_2=21.4 mm, L=60 mm and x_m=52 mm, corresponding to area contraction ratio $CR = 21.8$, for $c_H = 0$ and $c_S = 0$ as function of different Reynolds numbers in the range $300 \le Re \le 17{,}000$ (symbols). The vertical dashed-dotted line indicates the matching point of the cubics $x = x_m$. The scaled radius of the nozzle is indicated by a solid thick line.

the shape factor $H(\lambda)$ and the skin friction parameter $S(\lambda)$ the variation of the Thwaites parameter λ throughout the nozzle, shown in Fig. 7(*e*), can be neglected so that $\lambda \approx 0.0015$ holds for all streamwise positions and for all assessed Reynolds numbers.

The wall shear stress τ is estimated following Eq. (9) as $\tau = S(\lambda)\nu\rho U_c/\delta_2$. The physical fluid properties ρ and ν are constant and the skin friction parameter $S(\lambda)$ can be approximated by the constant value $S \approx 0.2$ regardless the Reynolds number.

Consequently, estimated values for τ are proportional to the ratio of the modeled centerline velocity U_c and the momentum thickness δ_2 since both quantities depend on the streamwise position x as well as on the Reynolds number Re as seen from Fig. 7(*a*) and Fig. 7(*d*). The estimated wall shear stress τ normalized by the pressure difference due to the contraction assuming an ideal fluid ΔP:

$$\Delta P \approx \frac{\rho}{2} U_1^2 \left(CR^2 - 1\right) \tag{19}$$

$$\approx \frac{\rho \nu^2}{2} \frac{Re^2}{D_2^2} \left(1 - \frac{1}{CR^2}\right) \tag{20}$$

is shown in Fig. 7(*h*). The maximum wall shear stress is seen to occur at a streamwise position located between the position of maximum acceleration and the nozzle exit where the streamwise velocity is maximum. For all assessed Reynolds numbers it is observed that the estimated wall shear stress is of the same order of magnitude as the pressure difference imposed by the contraction since the normalized wall shear stress varies between 0.5 and 5.5. For Reynolds numbers in the range $Re > 6000$ the pressure difference is more important than the wall shear stress as seen from $0.5 < \tau/\Delta P < 1$. For Reynolds numbers $3000 < Re < 6000$ the normalized wall shear stress increases in the range $1 < \tau/\Delta P < 2$. For Reynolds numbers $Re < 3000$ the ratio increases further so that $\tau/\Delta P > 2$ holds indicating that viscous fluid forces becomes predominant, which is in accordance with the findings described for the centerline velocity U_c, the displacement thickness δ_1 and the momentum thickness δ_2. Moreover, it is noted that although the variation in the magnitude of the shape factor $H(\lambda)$ and the skin friction parameter $S(\lambda)$ are to small to be significant, the observed tendencies, i.e., increase of H and decrease of S for decreasing Reynolds number, are in accordance with the loss of relative importance of the pressure gradient ΔP to the wall shear stress τ.

5.2 Modeled and Measured Exit Centerline Velocity. In Sec. 5.1 the modeled flow throughout the nozzle is described. The modeled quantities show that a contraction nozzle with area contraction ratio $CR = 21.8$ defined by the geometrical parameter set $D_1 = 100$ mm, $D_2 = 21.4$ mm, $L = 60$ mm, and $x_m = 52$ mm enables to obtain flow uniformity at the nozzle exit while flow separation upstream the nozzle exit is avoided. In the current section the influence of the nozzle diameters (D_1, D_2) on the model outcome is sought for fixed values of the total nozzle length $L = 60$ mm and the matching point $x_m = 52$ mm. The assessed nozzle diameters (D_1, D_2) and corresponding area contraction ratio CR are listed in Table 2. It is seen that all assessed contraction ratios summarized in Table 2 are smaller than or of the same order of magnitude than $CR = 21.8$ for which no flow separation occurs. Since flow separation is favored by increasing the contraction ratio, it is assumed that no flow separation occurs for any of the geometries summarized in Table 2. The chosen values of D_1, D_2 and CR enable to assess the influence of each individual parameter of the set (D_1, D_2, CR) on the modeled flow outcome.

Table 2 Overview of varied parameters for contraction geometries defined in Eq. (1) and Eq. (2) for fixed matching position $x_m = 52$ mm and contraction length $L = 60$ mm: (I) constant inlet diameter D_1, (II) constant outlet diameter D_2, (III) constant contraction ratio CR and (IV) geometrical nozzle parameters used for experimental validation as detailed in Sec. 4

		D_1 [mm]	D_2 [mm]	CR [−]
Modeled	I (D_1)	100	21.2	22.2
		100	21.4	21.8
		100	21.6	21.4
	II (D_2)	100	25	16
		50	25	4
		50	21.6	5.4
	III (CR)	50	21.4	5.5
		45.4	21.4	4.5
		45.8	21.6	4.5
Experimental validation		100	21.4	21.8

Modeled centerline velocities at the nozzle exit U_2 normalized by the centerline velocity at the nozzle inlet U_1, i.e., U_2/U_1, for all assessed nozzle parameters are shown in Fig. 8. In addition, measured centerline velocities presented in Sec. 4 are plotted so that, for the nozzle characterized by the parameter set $D_1 = 100$ mm, $D_2 = 21.4$ mm, $L = 60$ mm, and $x_m = 52$ mm, modeled and measured values can be compared.

Figure 8(*a*) shows the influence of a variation of exit diameter D_2 for a fixed upstream diameter $D_1 = 100$mm on the ratio of exit and inlet centerline velocity U_2/U_1 as function of Reynolds number. The exit diameter D_2 is varied in the range from 21.2 to 25 mm corresponding to a variation of 10%. For an ideal fluid characterized by an uniform velocity profile throughout the nozzle, the ratio U_2/U_1 yields the area contraction ratio, *i.e.* $U_2/U_1 = CR$, which is determined by the geometry and independent of Reynolds number. From Fig. 8(*a*) is seen that the variation of the ratio U_2/U_1 becomes indeed smaller than 1% for Reynolds numbers $Re > 3000$. For Reynolds numbers $Re < 3000$ the boundary layer develops rapidly so that the ratio U_2/U_1 increases in accordance with observations made on Fig. 7(*a*). The ratio U_2/U_1 decreases as the exit diameter D_2 increases due to the decrease in contraction ratio CR. Modeled and measured velocity ratios U_2/U_1 are compared for $D_2 = 21.4$mm. The modeled U_2/U_1 ratios matches well with the measured U_2/U_1 values except for Reynolds numbers $Re < 3000$ in which case the modeled values underestimate the measured velocity ratios. The discrepancy between modeled and measured values increases from 1% for $Re \approx 3000$ to 20% for $Re < 1000$. Consequently, the applied model with parameters $c_{H,S} = 0$ looses accuracy as the boundary layer growths for $Re < 3000$ and becomes inaccurate for $Re < 1000$.

The influence of varying inlet diameter D_1 or exit diameter D_2 on the velocity ratio U_2/U_1 for different Reynolds numbers is discussed from Fig. 8(*a*) and Fig. 8(*b*). The geometrical parameters characterizing the experimental nozzle, $D_1 = 100$ mm and $D_2 = 21.4$ mm resulting in $CR = 21.8$, are taken as a reference. From Fig. 8(*a*) is seen that increasing the downstream diameter D_2 with ±1% and 17% decreases the predicted velocity ratio U_2/U_1 with ±3% and 27%, respectively. From Fig. 8(*b*) is observed that reducing the inlet diameter D_1 with 50% and maintaining a variation of the upstream diameter D_2 with 1% and 17% from its reference value, reduces the influence of varying the downstream diameter D_2 from its reference value to 1% and 12%. Consequently, the influence of a variation in exit diameter D_2 on the model outcome increases as the inlet diameter D_1 increases. Moreover, it is seen that reducing the inlet diameter $D_1 = 100$ mm with 50%, which corresponds to dividing the contraction ratio CR by 4, decreases the ratio U_2/U_1 by a factor greater than 4 or a decrease >25% illustrating the influence of reduced flow acceleration as the contraction ratio decreases.

In Fig. 8(*a*) and Fig. 8(*b*) the nozzle parameter D_2 is varied with ±1% for a fixed value of $D_1 = 100$ mm so that a small variation of 2% on the area contraction ratio CR is imposed. Figure 8(*c*) shows the model outcome U_2/U_1 for the same variation of 1% on the exit diameter D_2 and a constant area contraction ratio $CR = 4.5$ which is obtained by increasing the inlet diameter D_1 with less than 1%. From Fig. 8(*c*) is seen that the increase in inlet and outlet diameter results in an increase of 1% in the ratio U_2/U_1 for all Reynolds numbers Re which is also observed in Fig. 8(*b*) in case only the exit diameter D_2 is increased. Consequently, small variations <1% of the inlet diameter D_1 do not influence the model outcome for U_2/U_1.

Figure 8(*d*) shows the influence of the model parameters $c_{H,S}$ on the model outcome as function of Reynolds numbers. The model constants are introduced in Eq. (7) for the boundary layer shape factor $H(\lambda)$ and in Eq. (6) for the skin friction parameter $S(\lambda)$ in order

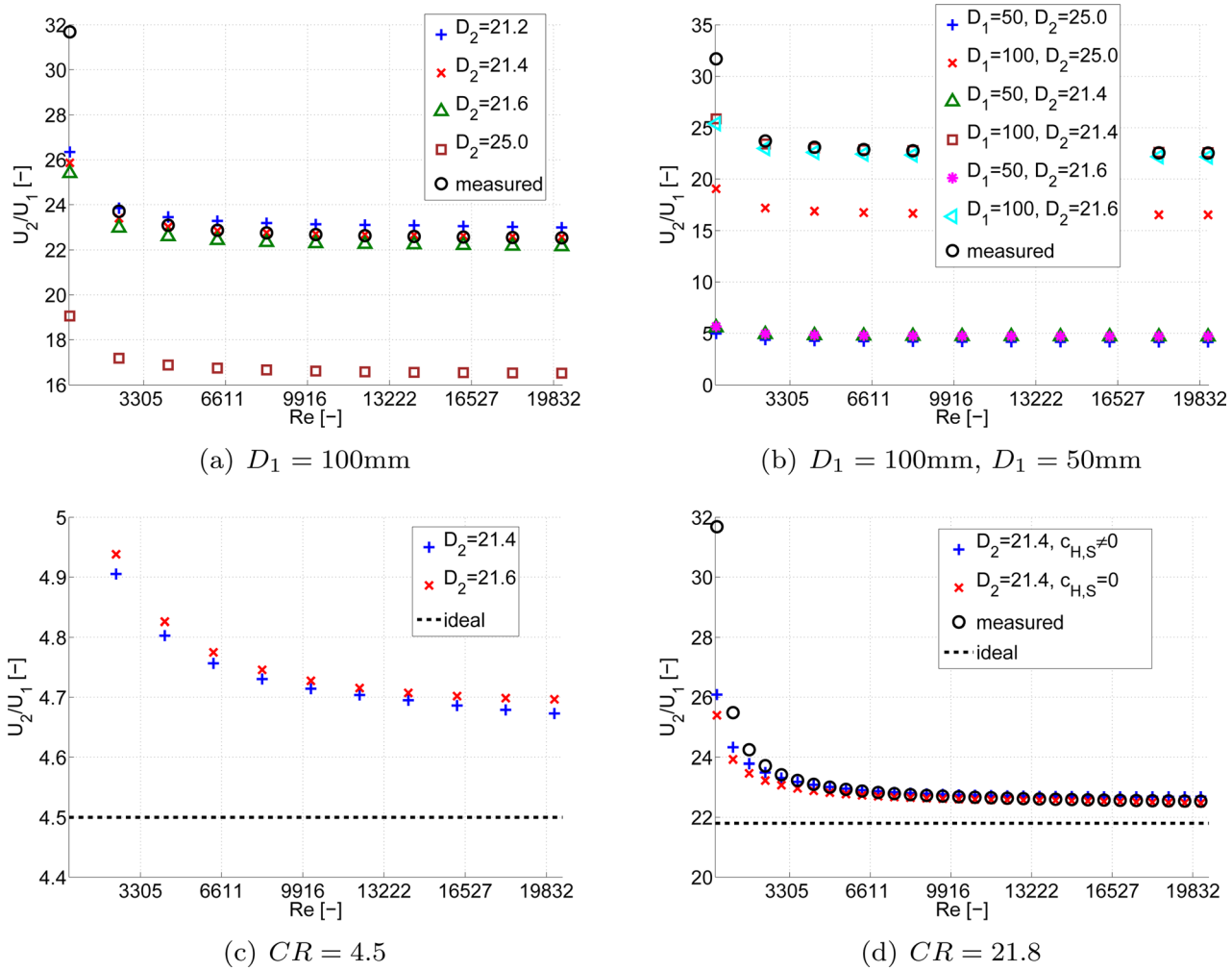

Fig. 8 Modeled and measured centerline velocity at the nozzle exit normalized by the inlet centerline velocity U_2/U_1 as function of Reynolds number *Re* for (*a*) fixed inlet diameter $D_1 = 100$ mm, (*b*) inlet diameter $D_1 = 100$ mm and $D_1 = 50$ mm, (*c*) fixed area contraction ratio $CR = 4.5$ and (*d*) fixed area contraction ratio $CR = 21.8$. The ratio U_2/U_1 for an ideal fluid yields the area contraction ratio *CR* (dashed line labeled ideal). Measured centerline velocities for $D_1 = 100$ mm and $D_2 = 21.4$ mm are indicated (measured). Modeled values are obtained for $c_H = 0$ and $c_S = 0$, denoted $c_{H,S} = 0$, except in Fig. 8(*d*) where also results for $c_H = 0.35$ and $c_S = -0.02$, labeled $c_{H,S} \neq 0$, are shown.

to determine their dependence on the Thwaites parameter λ. The nozzle geometry is characterized by the reference values for the geometrical parameters, $D_1 = 100$ mm and $D_2 = 21.4$ mm and therefore $CR = 21.8$, corresponding to the nozzle used for experiments described in Sec. 4. The model outcome obtained for zero model parameters $c_{H,S} = 0$ is compared to the model outcome obtained for non zero model parameters $c_{H,S} \neq 0$. The choice of non zero model parameters $c_H = 0.35$ and $c_S = -0.02$ is motivated in Sec. 3. For completeness also the constant value $U_2/U_1 = CR$ is shown in Fig. 8(*d*) which provides an underestimation of a boundary layer model since it assumes an ideal fluid characterized by a uniform velocity profile for which boundary layer development is neglected. From Fig. 8(*d*) is seen that the influence of zero or non zero constants $c_{H,S}$ on the model outcome can be neglected for Reynolds numbers $Re > 6000$ for which the discrepancy between the modeled values is less than 1%. As the Reynolds number is decreased the discrepancy increases to <3% in the range $6000 > Re > 3000$ and up to 15% for $3000 > Re > 300$. Consequently, the choice of model parameters $c_{H,S}$ determines the model outcome in the range $300 < Re < 3000$. In order to evaluate the choice of model parameters $c_{H,S}$ for the experimentally studied nozzle the model outcome is compared to the measured values for U_2/U_1. For Reynolds numbers $Re > 3000$ both zero and non zero model constants approximate the measured data to within 2% corresponding with the experimental error on the ratio U_2/U_1. For Reynolds numbers in the range $3000 > Re > 1000$ the accuracy of the model outcome reduces to within <7% for the use of zero constants and to within <4% for the use of non zero constants $c_{H,S} \neq 0$. For Reynolds numbers $Re < 1000$ the difference between measured and modeled U_2/U_1 ratios increases to more than 20% so that the model outcome is inaccurate for all assessed $c_{H,S}$ values.

5.3 Modeled and Measured Boundary Layer Characteristics at the Nozzle Exit. In the previous Sec. 5.2 the influence of geometrical parameters, inlet diameter D_1 and outlet diameter D_2, on the model outcome is assessed as well as the use of zero or non zero model constants c_H in Eq. (7) for the boundary layer shape factor $H(\lambda)$ and c_S in Eq. (6) for the skin friction parameter $S(\lambda)$. The model outcome is validated with respect to the centerline velocity U_2 on the measured centerline velocities. In the current section experimental validation of the modeled boundary layer characteristics at the nozzle exit is aimed using the transverse velocity measurements for the nozzle with geometrical parameters $D_1 = 100$ mm, $D_2 = 21.4$ mm, $L = 60$ mm, and $x_m = 52$ mm presented in Sec. 4. The boundary layer characteristics of interest are the displacement thickness δ_1, the momentum thickness δ_2, the shape factor $H = \delta_1/\delta_2$ and the Thwaites parameter λ given in

Eq. (8), Eq. (3), Eq. (7) and Eq. (5), respectively. The influence of model and experimental parameters on the estimated quantities is sought. As in Sec. 5.2, the influence of using zero or non zero model parameters $c_{H,S}$ on the predicted boundary layer characteristics is assessed. In addition, the influence of the spatial step size Δy between consecutive positions of the hot film probe used to measure the transverse profile is assessed. It is detailed in Sec. 4 that for the measured exit profile scanning the complete exit diameter the transverse positioning step size is $\Delta y = 0.1$ mm and that for the measured exit boundary layer profile scanning the boundary layer the transverse positioning step size is $\Delta y = 0.01$ mm.

Figure 9 shows the model predictions and experimental values for δ_1, δ_2, H, and λ at the nozzle exit as function of Reynolds number.

The experimental values are obtained by integration of the measured transverse velocity profiles following the equations outlined in Sec. 3. Estimated values for $\Delta y = 0.1$ mm overestimates the estimated values for $\Delta y = 0.01$ mm with more than 40%. Consequently, the size of the spatial step between consecutive transverse measurement positions determines the accuracy of the integration and therefore the error on the boundary layer characteristics δ_1 and δ_2 since the influence of a streamwise positioning error can be neglected based on the good match between the measured exit profile ($\Delta y = 0.1$ mm) and the measured boundary layer profile ($\Delta y = 0.01$ mm) as shown in Fig. 4(*a*). Therefore, imposing a spatial step which is smaller than the sensor diameter, $\Delta y < d_w$ as proposed in Sec. 4, is simple criterion to reduce the integration error for the non uniform portion of the measured velocity profile. Obviously, this criterion can only be applied in case a highly accurate positioning system is available. Note that the discrepancy between values predicted with both profiles reduces as the Reynolds number increases since the boundary layer thickness reduces so that the spatial step size becomes less important.

From Fig. 9(*b*) is seen that modeled values of the momentum thickness δ_2 do not depend on the applied model constants. On the other hand, modeled values of the displacement thickness δ_1 obtained for zero constants $c_{H,S} = 0$ underestimate the values obtained for non zero constants $c_{H,S} \neq 0$ with >10% for all Reynolds numbers.

Figure 9(*a*) and Fig. 9(*b*) show that for all Reynolds numbers $300 < Re < 20{,}200$ the modeled values of displacement thickness δ_1 and momentum thickness δ_2 obtained for non zero constants $c_{H,S} \neq 0$ are in close agreement with the experimental values derived on the measured boundary layer profile ($\Delta y = 0.01$mm). For Reynolds numbers $Re > 3000$ the discrepancy between modeled and experimental values is smaller than 2%. The discrepancy increases as the Reynolds number decreases due to boundary layer development to <4% in the range $3000 > Re > 1000$ and to <20%

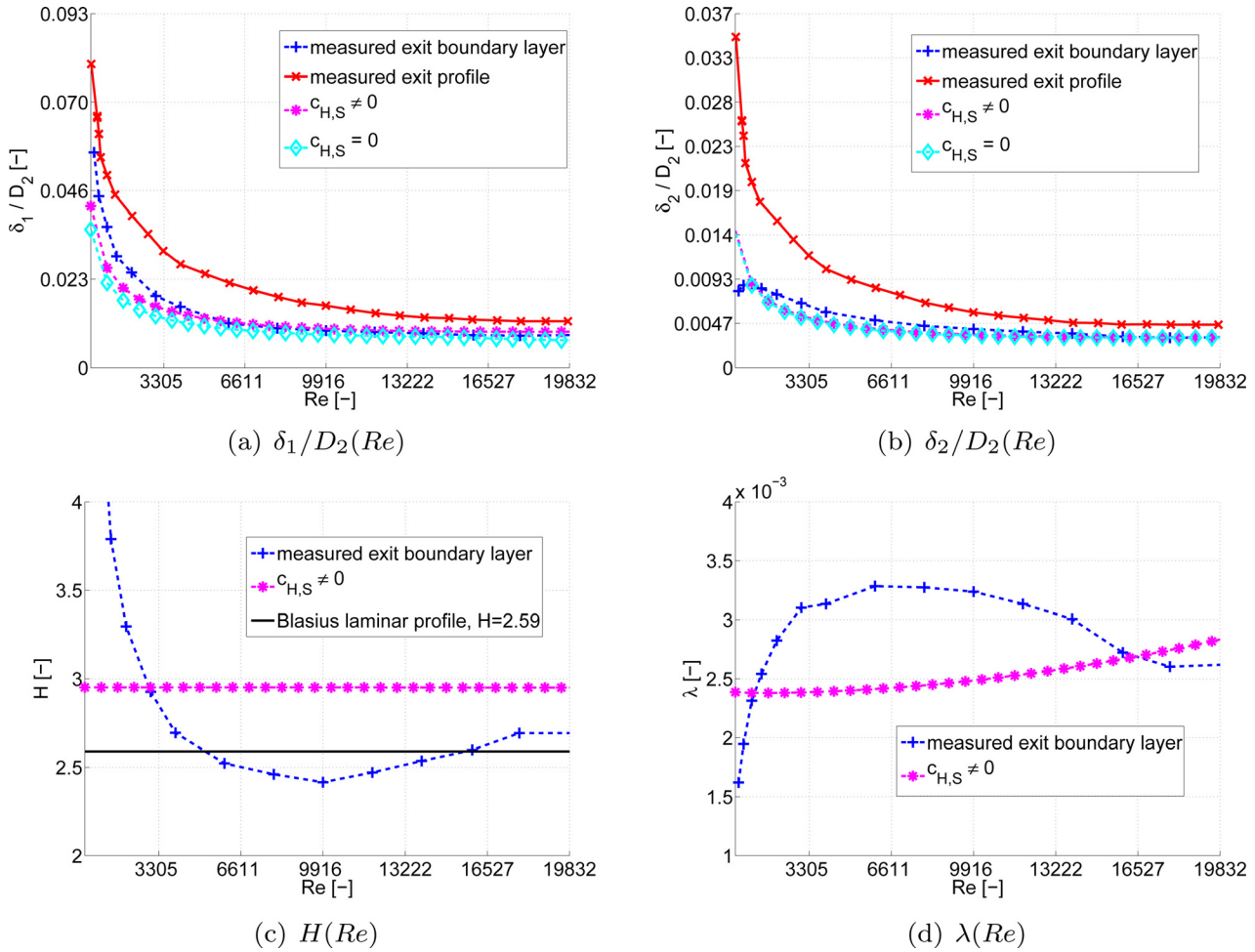

Fig. 9 Comparison of modeled and experimental assessed normalized boundary layer characteristics δ_1/D_2 (Fig. 9(*a*)), δ_2/D_2 (Fig. 9(*b*)), H (Fig. 9(*c*)) and λ (Fig. 9(*d*)) at the exit of the nozzle with parameters D_1=100 mm, D_2=21.4 mm, L=60 mm, and x_m=52 mm as function of Reynolds number. The influence of model coefficients $c_{H,S}$ and spatial step size Δy in the transverse exit profile is illustrated for δ_1 and δ_2. Zero model constants $c_H = 0$ and $c_S = 0$ is denoted $c_{H,S} = 0$ whereas non zero model constants $c_H = 0.35$ and $c_S = -0.02$ is denoted $c_{H,S} \neq 0$. Quantities estimated from transverse profiles using $\Delta y = 0.1$mm are labeled "measured exit profile" and transverse profiles using $\Delta y = 0.01$ mm are labeled "measured exit boundary layer." In Fig. 9(*c*) also the theoretical value $H = 2.59$ for Blasius laminar profile is shown.

for $1000 > Re > 300$. The mentioned errors increases with >10% when the experimental estimation of δ_1 is compared to the model outcome with zero constants. Consequently, the introduction of non zero model constants c_H in Eq. (7) for the boundary layer shape factor $H(\lambda)$ and c_S in Eq. (6) for the skin friction parameter $S(\lambda)$ as shown in Fig. 2 increases the model accuracy as the Reynolds number decreases as seen for the prediction of the centerline velocity discussed in Sec. 5.2 as well as for the prediction of the boundary layer thickness δ_1.

The displacement thickness δ_1 shown in Fig. 9(*a*) is approximately 0.9% of the nozzle exit diameter D_2 for Reynolds numbers in the range $Re > 3000$. For smaller Reynolds numbers the displacement thickness δ_1 increases rapidly to 3% for Reynolds numbers $3000 > Re > 1000$ and to 6% for Reynolds numbers $1000 > Re > 300$.

From Fig. 9(*b*) is seen that the momentum thickness $\delta_2 \approx 0.004 D_2$ varies little with Reynolds number in the range $Re > 3000$ so that using $\delta_2 = 0.004 D_2$ in the top hat velocity profile given in Eq. (18) allows to approximate the measured shape of the transverse velocity profile as shown in Fig. 4(*b*). For Reynolds numbers $300 < Re < 3000$ the momentum thickness increases rapidly to about twice this value, i.e., an increase with 50% to about 1% of the exit diameter D_2, so that $0.004 D_2 \leq \delta_2 \leq 0.01 D_2$.

An experimental estimation of the shape factor H and Thwaites parameter λ is obtained using the experimental estimations of δ_1 and δ_2 associated with spatial step size $\Delta y = 0.01$ mm. In Fig. 9(*c*) and Fig. 9(*d*) the experimental estimates for H and λ are compared to model predictions for non zero model constants $c_{H,S} \neq 0$. The experimental and modeled values for H are greater than 2.4 confirming the laminar nature of the flow. Since modeled δ_1 values are larger than experimental δ_1 values for $Re > 3000$, the modeled shape factor H overestimates experimental H values in this range of Reynolds numbers. For Reynolds numbers $Re < 3000$, the experimental boundary layer estimation shows a strong increase reflecting the increased displacement thickness due to strong boundary layer development. The small variation of modeled H values is due to the small variation of modeled λ values as shown in Fig. 9(*d*). The experimentally estimated λ values varies in the range covered by the modeled values. Consequently, the modeled and measured values for H and λ result in a same order of magnitude, but a quantitative comparison results in large errors between 20% and 40%.

6 Conclusion

Flow through a parameterized axisymmetrical contraction nozzle of limited size is studied for $300 < Re < 20{,}200$ based on transverse velocity measurements at the nozzle exit. The nozzle is characterized by the nozle exit diameter $D = 21.4$ mm, contraction ratio $CR = 21.8$ and total length $L = 6$ cm. Transverse exit velocity profiles are measured and the flow throughout the nozzle is modeled by implementing Thwaites axisymmetrical laminar boundary layer method in an iterative algorithm.

The following conclusions are made:

- For all assessed Reynolds numbers Re, the measured transverse mean exit velocity profiles show a satisfactory sharp top hat shape with uniform flow in the range $-0.25 < y/D < 0.25$. Outside the uniform center, in the range $|y/D| > 0.25$, the boundary layer is found to be laminar. The centerline turbulence intensity yields <1% for all assessed Reynolds numbers. The displacement thickness δ_1 yields about 0.9% of the exit diameter for $Re > 3000$. For $Re < 3000$, the boundary layer growths rapidly and δ_1 increases to 3% of the exit diameter in the range $1000 < Re < 3000$ and to 9% of the exit diameter for $300 < Re < 1000$. Consequently, the small nozzle provides low turbulence inflow with uniform core flow for Reynolds numbers in the range $300 < Re < 20{,}200$.
- Reducing the spatial step when scanning the transverse velocity in the boundary layer to less than the hot film diameter increases the accuracy of the measured displacement thickness δ_1 and momentum thickness δ_2 with more than 40% for all assessed Reynolds numbers since errors due to spatial integration are avoided.
- Two constants are introduced in the universal functions describing the skin friction parameter and the shape parameter in Thwaites laminar axisymmetrical boundary layer solution based on tabulated values reported in literature. The constants allow to extent the Reynolds number range for which the model is accurate, i.e., the discrepancy between modeled and measured values is less than 4%, from $3000 < Re < 20{,}200$ to $1000 < Re < 20{,}200$ for the centerline velocity as well as for the boundary layer characteristics δ_1 and δ_2. Consequently, the implementation of Thwaites laminar axisymmetrical boundary layer solution provides a simple algorithm to quantify the flow at the exit for Reynolds numbers in the range $1000 < Re < 20{,}200$. For Reynolds numbers $Re < 1000$ the model outcome provides a qualitative estimation since the error increases as the boundary layer develops.

Appendix A: Algorithm Outline

For a given volume flow rate Q and discretized geometry with area $A(x) = \pi R(x)^2$

$$A_i = \pi R_i^2 \quad \text{and} \quad 1 \leq i \leq L/\Delta x + 1 \tag{21}$$

with i the discretization index in the x direction, the algorithm is schematically given as follows:

Algorithm 1: Flow chart for Thwaites laminar axisymmetrical boundary layer approximation

Input: volume flow rate Q and discretised contraction geometry A_i
Output: centerline velocity $U(x)$, $\lambda(x)$, $H(x)$, $S(x)$, $\delta_1(x)$, $\delta_2(x)$ and $\tau(x)$
initialization: $U_0^i = Q/A_i$, $\delta_0^2 = 0$, $\delta_0^1 = 0$, $\lambda_0 = 0$;
for $1 \leq i \leq L/\Delta x + 1$ **do**
  while $|U_i^{est} - U_i^{old}| > \epsilon_U$ or $|\lambda_i^{est} - \lambda_i^{old}| > \epsilon_\lambda$ **do**
    $U_i = \frac{Q}{\pi (R_i - H(\lambda_{i-1})\delta_{2,i})^2}$;
    $\delta_{2,i}^2 = \frac{0.45\nu}{R_i^2 U_i^6} \Delta x \sum_{j=1}^{i} R_j^2 U_j^5 + \frac{\delta_{2,1}^2 R_0^2 U_1^6}{R_i^2 U_i^6}$;
    $\lambda_i = \frac{\delta_{2,i}}{\nu} \frac{U_i - U_{i-1}}{\Delta x}$;
    $\delta_{1,i} = \delta_{2,i} H(\lambda_i)$;
    $U_i = \frac{Q}{\pi (R_i - H(\lambda_i \delta_{2,i})^2)}$;
    $\lambda_i^{est} = \lambda^{old} - k_\lambda (\lambda_i^{new} - \lambda_i^{old})$;
    $U_i^{est} = U_i^{old} - k_U (U_i^{new} - U_i^{old})$;
    $\tau_i = \frac{\rho \nu U_i^{est}}{\delta_{2,i}} S(\lambda_i^{est})$;
  end
end

The relaxation parameters $k_U = 1 \times 10^{-3}$ and $k_\lambda = 6 \times 10^{-5}$, convergence parameters $\varepsilon_U = 1 \times 10^{-5}$ and $\varepsilon_\lambda = 1 \times 10^{-7}$ and discretization step $\Delta x = 2.6 \times 10^{-5}$m are chosen sufficiently small so that the simulation results are independent of their numerical value. The influence of the initialization parameters $U_i^0 = 0$, $\delta_2^0 = 0$, $\delta_1^0 = 0$ is largest in the uniform inlet portion of the nozzle, so that its influence can be neglected in the convergent portion.

Acknowledgment

The authors thank the Agence National de la Recherche France (ANR-09-BLAN-0376) for financial support.

Nomenclature

$[-]$ = dimensionless
ν = air kinematic viscosity $1.5 \times 10^{-5} m^2/s$

ρ = air density $1.2 kg/m^3$
D_1 = inlet diameter of axisymmetrical nozzle $[m]$
D_2 = exit diameter of axisymmetrical nozzle $[m]$
$R(x)$ = radius of the axisymmetrical nozzle $[m]$
$A(x) = \pi R(x)^2$ = area of the axisymmetrical nozzle $[m^2]$
L = total nozzle length in the x direction $[m]$
x_m = matching point required for parametrical description of the nozzle $[m]$
$CR = (D_2/D_1)^2$ = area contraction ratio of the nozzle $[-]$
Q = volume airflow rate $[m^3/s]$
$Re = \frac{4Q}{\nu \pi D_2}$ = bulk Reynolds number at the exit of the axisymmetrical nozzle $[-]$
x = longitudinal streamwise distance from nozzle inlet at $x = 0$ $[m]$
y = transverse distance from the centerline of the nozzle $[m]$
Δy = transverse step size for anemometry measurements $[m]$
$U_e(y)$ = transverse flow velocity profile at the exit of the nozzle $(x = L, -D_2/2 \le y \le D_2/2)$ $[m/s]$
$U_c(x)$ = centerline flow velocity $(0 \le x \le L, y = 0)$ $[m/s]$
U_1 = mean centerline velocity at the inlet of the nozzle $(x = 0, y = 0)$ $[m/s]$
U_2 = mean centerline velocity at the exit of the nozzle $(x = L, y = 0)$ $[m/s]$
U_2^p = instantaneous centerline velocity at the exit of the nozzle $[m/s]$
N_{tot} = total number of samples $[-]$
σ = second moment of velocity or root mean square $[m/s]$
T_U = local turbulence intensity $[-]$
$U(x)$ = flow velocity outside the boundary layer $[m/s]$
$u(x, y)$ = flow velocity in the boundary layer $[m/s]$
δ_2 = momentum thickness $[m]$
δ_1 = displacement thickness $[m]$
λ = Thwaites parameter $[-]$
τ = wall shear stress $[kg/ms^2]$
$S(\lambda)$ = skin friction parameter $[-]$
$H(\lambda)$ = boundary layer shape parameter $[-]$
$c_{S,H}$ = constants $[-]$
d_w = diameter of hot film $[m]$
T_a = room temperature $[^\circ C]$
$T_{a,r}$ = reference ambient temperature $[^\circ C]$
T_f = fluid temperature $[^\circ C]$
P_f = fluid pressure $[Pa]$
E_{meas} = measured hot-film output voltage $[V]$
E_{corr} = corrected hot-film output voltage $[V]$
p, i = auxiliary indices $[-]$
$\varepsilon_{U,\lambda}, k_{U,\lambda}$ = convergence and relaxation parameters $[-]$
N_{ind} = number of independent samples $[-]$
$U_\tau = \sqrt{\frac{\tau}{\rho}}$ = friction velocity [m/s]
U^+ = velocity normalized by friction velocity U_τ $[-]$
y^+ = Reynolds number based on friction velocity and distance from the nozzle wall $[-]$
ΔP = pressure difference imposed by the area contraction of the nozzle [Pa]

References

[1] Blevins, R., 1992, *Applied Fluid Dynamics Handbook*, Krieger, Malabar, FL.
[2] Kachhara, N., Wilcox, P., and Livesey, J., 1974, "A Theoretical and Experimental Investigation of Flow Through Short Axisymmetric Contractions," in *Proceedings of the 5th Australian Conference on Hydraulics and Fluid Mechanics*, pp. 82–89.
[3] Morel, T., 1975, "Comprehensive Design of Axisymmetric Wind Tunnel Contractions," J. Fluid Eng., **97**, pp. 225–233.
[4] Mikhail, M., 1979, "Optimum Design of Wind Tunnel Contractions," AIAA J., **17**, pp. 471–477.
[5] Metha, R., and Bradshaw, P., 1979, "Design Rules for Small Low Speed Wind Tunnels," Aeronaut. J. R. Aeronaut. Soc., **18**, pp. 443–449.
[6] Watmuff, J., 1986, "Wind Tunnel Contraction Design," in *Proceedings of 9th Australian Fluid Mechanics Conference*, pp. 82–89.
[7] Bell, J., and Mehta, R., 1988, "Contraction Design for Small Low-Speed Wind Tunnels," NASA STI/Recon Technical Report No. 89.
[8] Fang, F., 1997, "A Design Method for Contractions With Square End Sections," J. Fluid Eng., **119**, pp. 454–458.
[9] Fang, F., Chen, J., and Hong, Y., 2001, "Experimental and Analytical Evaluation of Flow in a Square-To-Square Wind Tunnel Contraction," J. Wind Eng. Indust. Aerodyn., **89**, pp. 247–262.
[10] Todde, V., Spazzini, P., and Sandberg, M., 2009, "Experimental Analysis of Low-Reynolds Number Free Jets: Evolution Along the Jet Centerline and Reynolds Number Effects," Exp. Fluids, **47**, pp. 279–294.
[11] Mi, J., Nobes, D., and Nathan, G., 2001, "Influence of Jet Exit Conditions on the Passive Scalar Field of an Axisymmetric Free Jet," J. Fluid Mech., **432**, pp. 91–125.
[12] Malmström, T., Kirkpatrick, A., Christensen, B., and Knappmiller, K., 1997, "Centreline Velocity Decay Measurements in Low-Velocity Axisymmetric Jets," J. Fluid Mech., **246**, pp. 363–377.
[13] Lee, T., and Budwig, R., 1991, "Two Improved Methods for Low-Speed Hot-Wire Calibration," Meas. Sci. Technol., **2**, pp. 643–646.
[14] Yue, Z., and Malmström, T., 1998, "A Simple Method for Low-Speed Hot-Wire Anemometer Calibration," Meas. Sci. Technol., **9**, pp. 1506–1510.
[15] Johnstone, A., Uddin, M., and Pollard, A., 2005, "Calibration of Hot-Wire Probes Using Non-Uniform Mean Velocity Profiles," Exp. Fluids, **39**, pp. 1432–1114.
[16] Daniloff, R., Schuckers, G., and Feth, L., 1980, *The Physiology of Speech and Hearing*, Prentice-Hall, Upper Saddle River, N.J.
[17] Shadle, C., 1985, "The Acoustics of Fricative Consonants," PhD thesis, Massachusetts Institute of Technology, Boston.
[18] Stevens, K., 1998, *Acoustic Phonetics*, MIT Press, London.
[19] White, F., 1991, *Viscous Fluid Flow*, McGraw-Hill, New York.
[20] Schlichting, H., and Gersten, K., 2000, *Boundary Layer Theory*, Springer Verlag, Berlin.
[21] Bruun, H., 1995, *Hot-Wire Anemometry*, Oxford Science, New York.
[22] Cebeci, T., and Cousteix, J., 2005, *Modeling and Computation of Boundary-Layer Flows*, Springer, Berlin.
[23] Thwaites, B., 1947, "On the Momentum Equation in Laminar Boundary-Layer Flow. A New Method of Uni-Parametric Calculation," Tech. Rep. No. 2587.
[24] Thwaites, B., 1949, "Approximate Calculations of Laminar Boundary Layers," Aeronaut. Quart., **1**, pp. 245–280.
[25] Rosenhead, L., 1963, *Laminar Boundary Layers*, Dover, U.K.
[26] Curle, N., 1962, *The Laminar Boundary Layer Equations*, Clarendon Press, London.
[27] Kavence, G., and Oka, S., 1973, "Correcting Hot-Wire Readings for Influence of Fluid Temperature Variations," DISA Info, **15**, pp. 21–24.
[28] Grandchamp, X., Van Hirtum, A., and Pelorson, X., 2010, "Hot Film/Wire Calibration for Low to Moderate Flow Velocities," Meas. Sci. Technol., **21**, pp. 1–5.
[29] Grandchamp, X., 2009, "Modélisation Physique des Écoulements Turbulents Appliquée aux Voies Aériennes Supérieures Chez L'humain," PhD thesis, Grenoble University, Grenoble.
[30] Benedict, L., and Gould, R., 1996, "Towards Better Uncertainty Estimates for Turbulence Statistics," Exp. Fluids, **22**, pp. 129–136.
[31] Michalke, A., and Hermann, G., 1982, "On the Inviscid Instability of a Circular Jet With External Flow," J. Fluid Mech., **114**, pp. 343–359.
[32] Zagarola, M., Perry, A., and Smits, A., 1997, "Log Laws or Power Laws: The Scaling in the Overlap Region," Phys. Fluids, **9**, pp. 2094–2100.